

Chapter 1

Functional modelling of idiopathic pulmonary fibrosis

In Chapter 4, HRCT based quantitative analysis and shape analysis methods were developed to provide a consistent way of describing the features and progressions of IPF disease. However, it is not clear how - or whether - the spatial distribution of tissue abnormalities in IPF (including classifications of tissue type) correlate with lung function and their change over time. Translating these imaging and shape bio-markers into functional bio-markers to directly help with clinical diagnosis and treatment is still a challenge in progress. For the patient with IPF, V/Q mismatching and hypoxaemia are frequent occurrences. Computational modelling provides a novel way to understand how changes to the lung tissue contribute to the decline of lung function, therefore modelling can be used to build a relationship between image-based bio-markers and functional presentations. This chapter outlines an approach to functional modelling of IPF. The quantitative tissue-level and shape-level features described in previous chapters were combined with pulmonary function tests (PFTs) to guide a patient-specific

computational model of lung function in IPF. The lung function of healthy older adults was also modelled for comparison with the IPF models. This chapter therefore aims to integrate data from volumetric imaging, PFTs, and computational models of lung function, to understand differences between IPF and normal older lungs. Lung function in IPF has been described in Chapter 2, and lung function in healthy older people will be introduced in Section 1.1.

1.1 Respiratory structure and function in older people

The respiratory system of the human keeps developing during the whole life, with the peak-point of pulmonary function achieved before 30 years of age (Janssens et al., 1999; Sprung et al., 2006). For most people, respiratory performance begins to gradually decline after reaching the maximal status. The ability of the lung to deliver more oxygen to tissues than they require ("reserve capacity") decreases by about four-fold from age 20 to age 70 in healthy people (Smith, 1986; Zaugg and Lucchinetti, 2000). Even in older athletes who experience vigorous endurance exercise and have better aerobic ability, the functional capability of the lung will progressively deteriorate over time (Mittman et al., 1965; Pollock et al., 1997; McClaran et al., 1995).

The ageing-related changes in respiratory physiology are usually associated with structural alterations in both lungs, dilatation of alveoli, enlargement of airspaces, decrease in gas exchange surface area, and increased residual volume (RV) and functional residual capacity (FRC) (Sprung et al., 2006; Lalley, 2013). There is a reduction in chest wall compliance and the static elastic recoil of the lung, which will lead to static air-trapping, decrease in vital capacity (VC), decrease in expiratory flows and increasing work of breathing compared with younger individuals (Sprung et al., 2006).

The strength of respiratory muscles decreases with age, and this is strongly correlated with nutritional status (lean body mass, body weight) and cardiac index (Janssens et al., 1999). The V/Q ratio heterogeneity tends to increase results from a closing of dependent airways, and carbon monoxide transfer capability also decreases which is associated with the reduced alveolar surface area. Interestingly, despite these changes, some research indicated that gas exchange may be preserved both at rest and during exertion, with only a slight reduction in arterial oxygen tension, and no significant change in arterial carbon dioxide tension, but pulmonary reserve is diminished (Janssens et al., 1999; Sprung et al., 2006). These age-associated changes are summarized and described in detail in Table 1.1.

1.1.1 Ageing-associated alterations in the chest wall and respiratory muscle function

Several morphological changes occur in chest wall and diaphragm in older people that reduce the capability and efficiency of the respiratory system. One of the most important changes is the progressive decline in chest wall compliance, which relates to the decrease of cross sectional area of the intercostal muscles, calcification of costal cartilage and rib-vertebral articulations, and narrowing of intervertebral disk spaces (Murphy, 1986; Crapo, 1993). The structural changes in the chest wall have been found to be associated with reduction in the curvature of the diaphragm and in the maximal trans-diaphragmatic pressure, however the thickness of the diaphragm seems not to change significantly in older adults (Zaugg and Lucchinetti, 2000; Sprung et al., 2006). It is noted that age-associated osteoporosis results in a shape change of the thorax geometry; that is, an increase in dorsal kyphosis and anterior-posterior chest diameter (Janssens

Table 1.1: Age-associated changes in respiratory function and their relationships to clinical presentations (Reproduced from (Sprung et al., 2006; Lalley, 2013))

Measurements	Changes, ≥ 60 yrs.	Clinical presentations
Static lung volumes		
- TLC	Unchanged	
- FRC	Increase	
- IRV	Modest increase	
- ERV	Increase	
- V_T	Modest increase	
- VC	Decrease	
- IC	Increase	
- RV	Increase	Impaired gas exchange
Dynamic lung volumes		
- FVC	Decrease	
- FEV ₁	Decrease	
- FEV ₁ /FVC	Decrease	
- Peak expiratory flow	Decrease	
Resistance and compliance		
- Respiratory system resistance	Increase	
- Small airways closure	Increase	Impaired gas exchange
- Chest wall compliance	Decrease	Increase in work of breathing
- Lung compliance	Increase	Decrease in ventilatory response to exercise
Respiratory (muscle) pressures		
- Mean pleural pressure	Unchanged	
- Respiratory muscle strength	Increase	
Gas transfer		
- Ventilation-perfusion mismatch	Increase	Impaired gas exchange
Altered control of breathing		
- Responsiveness to imposed respiratory loads	Decrease	Hypoventilation
- Responsiveness to hypoxemia and hypercarbia	Decrease	Hypoxemia and hypercarbia
- Sensitivity to anesthetic agents and opioids	Increase	Respiratory failure in early postoperative period

TLC: total lung capacity; FRC: functional residual capacity; IRV: inspiratory reserve volume; ERV: expiratory reserve volume; V_T : tidal volume; VC: vital capacity; IC: inspiratory capacity; RV: Residual volume; FVC: forced vital capacity; FEV₁ : forced expiratory volume in 1 s; FEV₁/FVC : the ratio of the forced expiratory volume in the first one second to the forced vital capacity of the lungs.

et al., 1999; Sprung et al., 2006).

The reduction in respiratory muscle strength caused by age-related decrease of maximal static inspiratory and expiratory pressures will lead to lower efficiency of respiratory muscle activity (Wijesinghe and Dow, 2005; Sprung et al., 2006; Lalley, 2013). It has been shown that the reduced respiratory muscle strength is associated with the deficient nutritional status in older people, and a strong relationship has been found between maximal inspiratory/expiratory pressure and lean body mass (Arora and Rochester, 1982; Janssens et al., 1999). Meanwhile, some studies have shown that the electromyographic signal produced by twitch stimulation decreases by around 50% in 70-year-olds compared with young subjects, and this reduction is attributed to the loss of type II fast-twitch muscle fibres (Larsson, 1983).

1.1.2 Ageing-associated alterations in pulmonary mechanics and lung volumes

Although the chest wall becomes stiffer in older people, their lung parenchyma actually become more compliant (Mittman et al., 1965; Turner et al., 1968; Zaugg and Lucchinetti, 2000). The elastic recoil pressure of lung tissue gradually reduces with ageing, at a rate of around 0.1 to 0.2 cmH₂O on average every year (Turner et al., 1968), and this reduction is attributed to the alterations in the spatial distribution of the elastic fibre network (Sprung et al., 2006). In older people, it can be observed that the static pressure-volume curve of the lung is shifted to the left; in contrast, the pressure-volume curve of the thorax is shifted to the right (Zaugg and Lucchinetti, 2000; Sprung et al., 2006).

The tidal volume experiences a slight decrease with ageing, whereas the respiratory

rate gradually increases (Sprung et al., 2006). As mentioned in Section 1.1.1, the chest wall becomes stiffer with ageing, while the lung tissues become more compliant. These changes will lead to an increase in RV and a decrease in VC (Lalley, 2013). Some research indicates that RV will increase by approximately 50% from a 20-year-old to a 70-year-old on average, and VC will drop to around 75% of the peak value during this period, with a decrease of 20 to 30 ml per year (Janssens et al., 1999; Sprung et al., 2006). The TLC, which is the air volume in the lungs during a maximum respiratory effort, remains unchanged with age, as the effect of the decreased inward elastic recoil of the lung is offset by the reduction in the outward elastic recoil of the chest wall (Sprung et al., 2006). However, the FRC increases by 1 to 3% per decade, since the rate of decrease in lung recoil exceeds the rate of decrease in chest wall compliance (Janssens et al., 1999; Lalley, 2013). Forced vital capacity (FVC) and forced expiratory volume in one second (FEV_1) have been demonstrated to decrease progressively with ageing in both men and women (Knudson et al., 1976), but the volumes reduce more rapidly in males than in females (Crapo, 1993). FEV_1 decreases by 20 approximately ml per year in subjects aged 25 to 29 years, but for people more than 65 years old, the average annual rate of reduction is more dramatic: up to 38 ml (Brandstetter and Kazemi, 1983).

1.1.3 Ageing-associated alterations in gas exchange

The inhomogeneity or "mismatch" of ventilation and perfusion increases with age, especially in the gravitationally dependent regions of the lung where intrapleural pressure becomes higher with age, and as the lung tissues become less elastic, they fail to keep small airways open (Holland et al., 1968; Paoletti et al., 1985; Lalley, 2013). The increased ventilation-perfusion heterogeneity results in a reduction in P_aO_2 , with a pro-

gressive drop from approximate 95 mmHg at 20 years to about 75 mmHg at 70 years. However, PaCO_2 remains almost unchanged with increasing age, although PaO_2 declines (Wahba, 1983; Sprung et al., 2006). This can probably be explained by the decreased rate of basal metabolism and the higher diffusive capability of CO_2 across the alveolar-capillary membrane (Levitzky, 1984). Local pulmonary perfusion can also reduce with age in some regions that are well ventilated as a result of reduced cardiac output (Levitzky, 1984; Lalley, 2013). The alveolar-arterial pressure difference for oxygen ($P_{\text{A}-\text{a}}\text{O}_2$) increases with ageing due to the increased heterogeneity of V/Q, and is probably also related to the increase in closing volume during breathing (Janssens et al., 1999). It can be observed that PaO_2 reduces at a rate of approximately 5 mm Hg per decade from the age of 20 years. Additionally, the diffusing capacity of the lungs for carbon monoxide (DLCO) decreases with age (Guenard and Marthan, 1996), with loss of about $0.3 \text{ mL} \cdot \text{min}^{-1} \text{ mmHg}^{-1}$ and $0.2 \text{ mL} \cdot \text{min}^{-1} \text{ mmHg}^{-1}$ per year for men and women, respectively (Murray, 1986). The reduction is more significant after 40 yrs of age, and the increased mismatch in V/Q, a decline in the alveolar surface area (Verbeken et al., 1992; Thurlbeck and Angus, 1975), the decreased density of lung capillaries (Butler and Kleinerman, 1970) and the reduction in pulmonary capillary blood volume (Guenard and Marthan, 1996) are all potential factors to cause the reduced diffusion capacity.

1.1.4 Relationship between lung function and lung shape

There is strong evidence that age-related changes in lung structures are associated with a series of alterations in respiratory function (introduced in Section 1.1). For example, the reduction in chest wall compliance of older people leads to a decrease in VC, while an

increased RV in the elderly usually results in impaired capability of gas exchange which relates to a lower measured DLCO. In a previous study (Osanlouy, 2018), several lung structure-function relationships were analysed through quantifying the correlations between the first three PCA-based mode weights calculated for a SSM of a healthy cohort aged 20-90 years with age, BMI, lung volume and some pulmonary function measurements. For each training subject of this SSM, the individual weight scores for each of the first three shape modes (which captures most shape variation) were examined. An ordinary least squares regression was applied to test the associations, and the P value was used to quantify the strength of each association, with an alpha level of 0.05 considered statistically significant. Analysis showed that Mode 1 is positively correlated with FEV₁, FEV₁/FVC, Maximal mid-expiratory Flow (FEF25%-75%), BMI and DLCO, whereas it is negatively correlated with age, RV and RV/TLC. For Mode 2, only BMI was found to be correlated with the shape variation, whereas quite a number of lung volume measurements (including FRC, TLC ,VC and RV) showed strong relationships with Mode 3.

1.2 Methods: Patient-specific modelling of IPF lung function

In this section, a patient-specific computational model of lung function is proposed to explore V/Q matching and whole lung gas exchange for patients with IPF. In order to make a comparison of lung function between the IPF patient and older normal people, for each patient, a subject-specific lung mesh that represents the statistical lung shape of a normal individual of the same age, BMI and pulmonary functional data was predicted

using an SSM. Anatomically-based airway and blood vessel trees were generated from HRCT images of IPF subjects, and for the corresponding normal lung mesh. Ventilation, perfusion, and gas exchange were simulated in the IPF and control models under baseline healthy conditions, and with constriction of airways and/or blood vessels in tissue regions classified as abnormal. To achieve this, the individual's lung parenchymal tissue classification and quantification data was mapped to their spatial model, with fibrosis assumed to reduce tissue compliance and narrow vessels. Data from PFTs were used to parameterize the models and set the boundary conditions for simulation. The modelling framework is illustrated in Figure 1.1.

1.2.1 Clinical data

Two patients diagnosed with IPF were selected from the clinical data used in Chapter 4 as representative subjects for functional modelling. Patient 1 is female with three imaging time points at 0, 12 and 23 months, and patient 2 is a male with two time points at 0 and 46 months. The clinical data for each patient includes both HRCT images and PFT results, with less than 3 months between the scan date and the PFT date.

1.2.2 Construction of lung lobe geometry

In Chapter 4, Section ?? and ??, the lung lobe shapes and volumes of an IPF cohort were compared with a normal older (control) cohort. It was shown that there is a significant difference of lung lobe geometry between IPF and older controls, and this alteration in lung shape is mainly in the basal region (lower lobe), which is strongly associated with the distribution of fibrosis in IPF. In order to include the impact of shape change into the modelling of lung function, a SSM of a normal older cohort and the IPF patient's

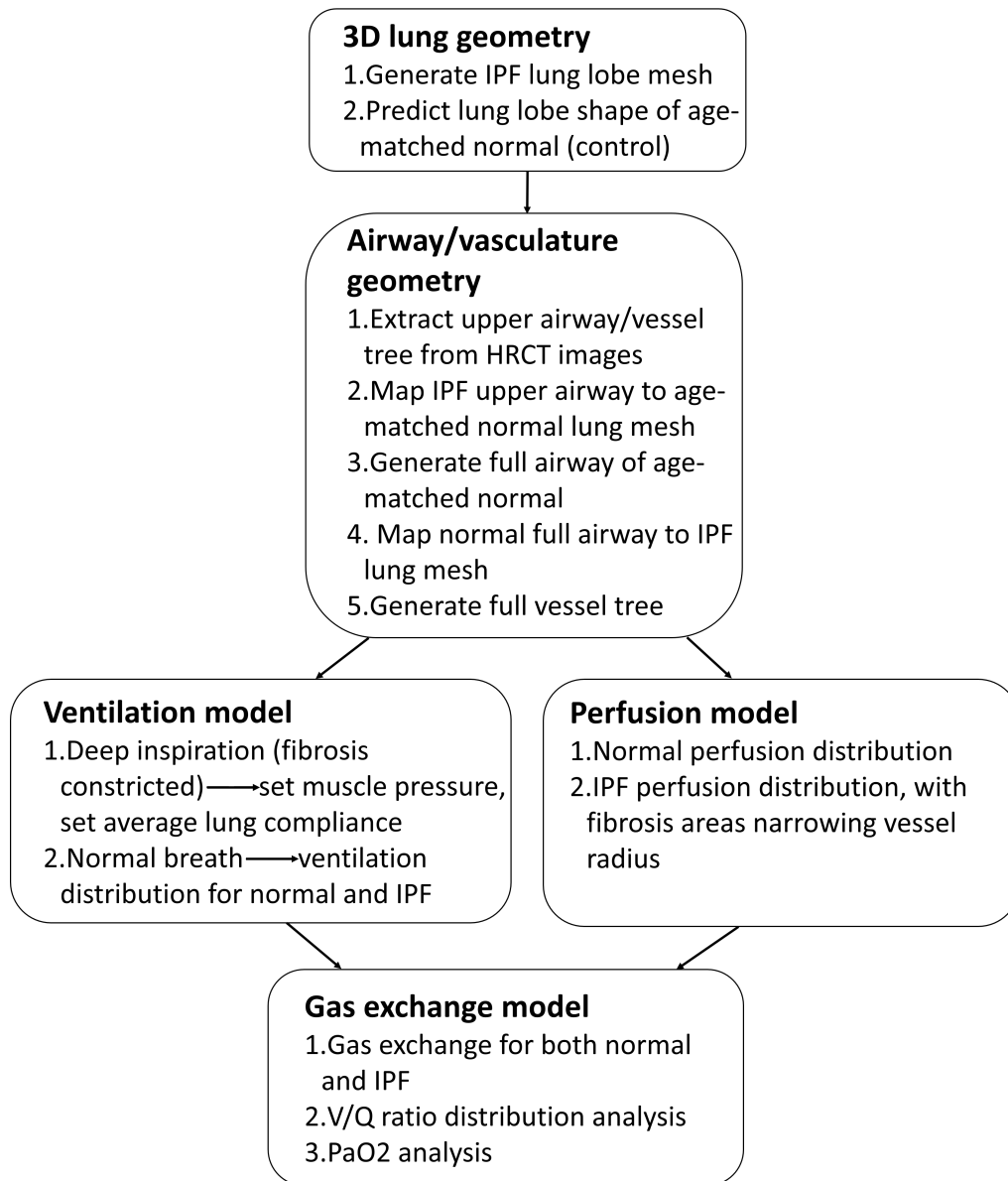


Figure 1.1: Computational modeling framework for IPF and older normal lung function.

individual information were combined to predict a lung lobe shape model of an age-matched normal as a control model for both IPF patients. The lung lobe mesh of each IPF patient was generated using the method introduced in Chapter 3, Section ??.

The SSM used to predict the age-matched control model in this chapter is different from Osanlouy (2018), because it only includes subjects aged 50 years and over. Underlying relationships with lung function are still expected to be present, however.

Shape prediction of old normal lungs

A lung shape prediction model for a healthy cohort aged ≥ 50 years was developed based on a previous analysis of lung structure-function relationships (Osanlouy, 2018). Age, BMI, FVC, FEV_1 , FRC, TLC, VC, RV, RV/TLC and DLCO were selected as the individual functional measurements to train the lung shape predictive model, as these parameters have been shown to have relatively strong correlations with the first three shape modes. The training process for the lung shape predictive model was to find optimized equations that best describe the relationship between the functional measures and the mode weights. For each shape mode, a multivariate regression model was constructed as:

$$w_i = \alpha_{0i} + \alpha_{1i}m_1 + \alpha_{2i}m_2 + \dots + \alpha_{ni}m_n + \varepsilon, \quad (1.1)$$

where w_i is the weight score of the i th shape mode, n is the number of functional measures, $\alpha_{0i}, \alpha_{1i} \dots \alpha_{ni}$ are the regression coefficients (in which α_{0i} is the intercept) m_i is the tested value of the i th functional measure, and ε is a random error.

Using Equation 1.1, a set of possible regression models can be developed for each shape mode (with different regression coefficients $\alpha_{0i}, \alpha_{1i} \dots \alpha_{ni}$). In order to find the

best predictive model from all the possible models, the two most common criterions for model selection-the Akaike information criterion (AIC) and the Bayesian information criterion (BIC)-were used to deal with the trade-off between the goodness of fit of the model and the simplicity of the model. Both AIC and BIC are founded on information theory, with each calculated by:

$$AIC = 2k - 2\ln L(\theta), \quad (1.2)$$

$$BIC = \ln(n)k - 2\ln L(\theta), \quad (1.3)$$

where k is the number of the estimated parameters (that is the number of functional measures in this study) in the model, $L(\theta)$ is the maximized value of the likelihood function of the model and θ are the parameter values that maximize the likelihood function.

The multivariate regression models with the lowest values of AIC and BIC were selected as the best predictive models, then the models of the first three PCA modes were constructed in the form of Equation 1.1, as follows:

$$\begin{aligned} w_1 &= 1.38 + (-0.04 \times Age) + (0.38 \times FVC) + (-0.04 \times DLCO), \\ w_2 &= 3.49 + (-0.16 \times BMI) + 0.02 \times RV/TLC, \\ w_3 &= 4.90 + (-0.02 \times Age) + (-0.45 \times TLC) + (-0.05 \times DLCO), \end{aligned} \quad (1.4)$$

where w_1 , w_2 and w_3 are the weight scores of the first three shape modes. Through inputting the individual functional measures into the regression models, the weights of first three modes can be calculated. Then the subject-specific predicted shape of the

control lung model can be reconstructed by adding the linear combination of the first three modes to the average SSM:

$$S_{pred} = S_{mean} + \sum_{i=1}^3 \mathbf{u}_i w_i, \quad (1.5)$$

where S_{mean} is the mean of the SSM for the older normal cohort, and S_{pred} is the subject-specific predicted lung shape.

1.2.3 Construction of airway/vascular geometry

Subject-specific conducting airway trees and pulmonary vasculature trees were constructed for both IPF and control models. The geometry of the pulmonary airway and vessels are important subject-specific features. In this study, airway/vessel trees were first generated for the predicted control model, which represents a healthy lung matched to the IPF subjects. The models were then deformed to the shape of the IPF lung mesh which has quantifiable shape differences as described in Chapter 4. The airway/vasculature diameters were assigned to each branch as a postprocessing step, with values appropriate for a healthy lung and for IPF. In this way, the branches for the IPF and control airway/vascular models retain the same geometric connectivity and same lobar distribution, but have different radius and length.

Airway tree

In order to generate an airway tree in the lung shape, the bi-cubic Hermite finite element mesh of the lung surface was converted to a tri-cubic Hermite volumetric mesh (introduced in Chapter 4, Section ??). An anatomically-based structure of the bronchial airways (from trachea to terminal bronchioles) was generated using the methods de-

scribed in detail in Tawhai et al. (2004). In brief, the centrelines of the largest airways (trachea, and left and right branches of the first 6 generations of airways) were manually segmented from the subject's HRCT images. This provides an incomplete description of the airway tree. Then, the larger airways were used as an initial condition to generate the remaining branches down to the level of the terminal bronchioles within the subject's lung mesh using a volume-filling branching algorithm. The steps to generate patient-specific airways in IPF and old normal lungs are summarized as follows:

1. 1-D finite element mesh of the centrelines of IPF larger airways were created manually from HRCT raw images of the IPF patient (shown in Figure 1.2a).
2. The 1-D tree of central airways was mapped to the volumetric mesh of the control model. The nodal positions inside the control mesh were mapped by calculating the local coordinate ξ_i with respect to its element (details in Chapter 4, Section ??). The branches outside the mesh were then scaled to match the target lung volume, followed by a manual adjustment. The element connectivity remained the same during mapping.
3. The mapped larger airways in step 2 was used as a starting geometry for generating a full airway tree by using a volume-filling branching algorithm (Tawhai et al., 2004), to fill the shape of the control mesh. Briefly, a uniformly-spaced grid of seed points was created within the 3D volumetric lung mesh. The number of seed points was ~ 32000 (45% for left lung and %55 for right lung) which approximates the number of pulmonary acini in the lung (Haefeli-Bleuer and Weibel, 1988). The branching algorithm was designed to generate a branching structure recursively towards the center of mass of seed point groupings, until each seed point was assigned to a terminal bronchiole (shown in Figure 1.2b).
4. The generated linear mesh of the full airway tree in step 3 was mapped back to the volumetric lung mesh of the IPF patient using the same method as in step 2.

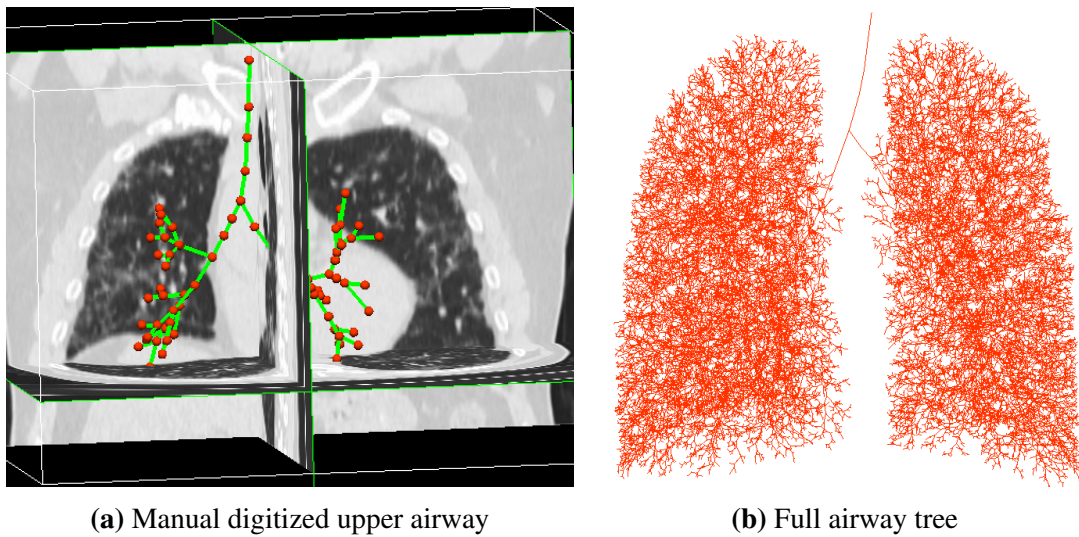


Figure 1.2: Generation of airway tree. (a) Manual digitized upper airway tree from HRCT images in 3D. Blue lines are the centerlines of upper airway tree, and red points represent airway nodes. (b) Geometry of full conducting airway tree generated using volume-filling algorithm. The model is shown from the anterior view, with the left lung on right, and right lung on left.

In the next stage, the diameters of the airway branches were assigned for both IPF and control models. The method was:

1. The trachea radius for IPF was measured from segmented HRCT images (based on the segmented cross-section of larger airway branches) at 25%, 50%, and 75% along the centreline of the trachea. The trachea radius was defined as the average of the three measurements.
2. The radius of the terminal bronchioles in the control models were assumed to be 0.2mm (Horsfield et al., 1976). The airways in the IPF lung have been found to be narrowed in 70% of patients (Crystal et al., 1976). The terminal bronchiole radius for the IPF models was therefore scaled to a smaller value. The scaling was assumed to be in proportion to the ratio of IPF to control model volumes, as:

$$R_{TB_{IPF}} = R_{TB_{Control}} \times \sqrt[3]{\frac{FRC_{IPF}}{FRC_{Control}}}, \quad (1.6)$$

where FRC_{IPF} is the measured FRC volume for the IPF patient and $FRC_{Control}$ is the reference FRC volume for the control model, $R_{TB_{IPF}}$ is the terminal bronchiole radius in the IPF models, and $R_{TB_{Control}} = 0.2\text{mm}$ is the terminal bronchiole radius in the reference (i.e. control) model.

3. The radii of the other airway branches for the IPF models were calculated by assuming a constant Horsfield diameter ratio (R_dH) for each IPF subject. R_dH is the rate of reduction of diameter (or radius) with reduction in Horsfield order, with R_dH calculated by:

$$R_dH = \frac{10 \times (\log_{10} R_{TB} - \log_{10} R_{Trachea})}{1 - R_oH}, \quad (1.7)$$

where R_{TB} is the terminal radius, $R_{Trachea}$ is the trachea radius, and R_oH is the Horsfield order of the airway model.

4. While the R_{TB} is expected to be smaller in IPF (Crystal et al., 1976), the anatomical deadspace (V_D) is actually larger (Plantier et al., 2016). $R_{Trachea}$ and R_dH for the control models were therefore set such that V_D (control) $< V_D$ (IPF), for $R_{Trachea}$ within the normal published range for men (6.5-12mm) and women (5-11mm) (Breatnach et al., 1984). V_D (control) was initialized using V_D (control) $= V_D$ (IPF) $\times (34.2/45.3)$, which is a relationship measured by Plantier et al. (2016) for IPF and controls. $R_{Trachea}$ and R_dH were adjusted until $R_{Trachea}$ was within the normal size range.

Using the above steps, a patient-specific pulmonary airway geometry for IPF and the control lung were constructed.

Vascular tree

The centrelines of the first two generations of vessel trees were manually segmented from HRCT images, and represented as a 1-D finite element mesh. In this thesis, the pulmonary arterial and venous trees of other generations were assumed to be approximate replicas of the airway tree. Using the airway tree to approximate vessel geometry is a reasonable assumption at this level, as the conventional pulmonary arteries generally follow the same branching pattern as the airways trees, and the airways and blood vessels have similar lengths and orientations. The airway and vasculature have been observed to bifurcate in union from larger branches to the bronchiole level, and the veins to divide at the approximate midpoint between adjacent airway bifurcations (Weibel, 1984; Hsia et al., 2016). The manually-segmented main vessels plus the finite element model of the airway tree provided a full pulmonary blood vessel geometry for the IPF patient. The vascular structure for the control model was obtained using the same mapping procedure used for the airways as described previously. The microcirculatory model of Clark et al (Clark et al., 2010, 2011) was appended to each terminal arteriole, to supply a corresponding terminal venule. Thus model is a symmetric-branching system of arterioles and venules that are connected (from arteriole to venule) at each generation by a recruitable and distensible "capillary sheet".

The unstrained (zero transmural pressure (P_{tm})) radius of the main pulmonary artery ($R_{mArtery}$) and vein (R_{mVein}) were assigned based on the patient-specific (measured) trachea radius and data from morphometric studies (Equation ??) (Horsfield, 1978; Horsfield and Gordon, 1981; Huang et al., 1996). The radius of all other arteries and veins down to the distal level were calculated based on a defined rate of increase in diameter with vessel Strahler order, the Strahler diameter ratio for artery and vein (R_dS_{Artery}

and R_dS_{Vein}). The value of R_dS for the arterial tree and venous tree were specified according to the radius of the main artery and vein, and aiming for consistency with published human data (Horsfield et al., 1971; Horsfield, 1978; Horsfield and Gordon, 1981; Huang et al., 1996):

$$R_{mArtery} = \frac{k_{Artery} \times R_{Trachea}}{R_{Trachea_{ref}}}, \quad (1.8)$$

$$R_dS_{Artery} = \frac{10 \times (\log_{10} R_{sArtery} - \log_{10} R_{mArtery})}{1 - R_oS}, \quad (1.9)$$

$$R_{mVein} = 10 \times \log_{10} \left(\frac{k_{Vein} \times R_{Trachea}}{\log_{10} R_{Trachea_{ref}}} \right), \quad (1.10)$$

$$R_dS_{Vein} = \frac{10 \times (\log_{10} R_{sVein} - \log_{10} (k_{Vein} \times R_{Trachea}))}{3 - R_oS}, \quad (1.11)$$

where k_{Artery} is constant artery radius (equals to 11.53), k_{Vein} is a constant for vein radius (equals to 6.3), $R_{Trachea_{ref}}$ is a statistical reference trachea radius (equals to 9 mm), $R_{sArtery}$ is the target for smallest arteries (equals to 0.125 mm), R_{sVein} is the target for smallest veins (equals to 0.125 mm), and R_oS is the Strahler order of the artery model. The vessel radius for the IPF models and the control models were then calculated.

1.2.4 Construction of computational models

In this chapter, computational modelling of lung function integrates previously published models of ventilation (Swan et al., 2012), perfusion (Clark et al., 2010, 2011) and gas exchange (Swan and Tawhai, 2010) to simulate \dot{V}/\dot{Q} distribution and oxygen

and carbon dioxide exchange during tidal breathing in the upright posture. The patient-specific geometry of airways and vessels were used as input for these models. A brief introduction of the model components is summarized below, and details can be found in the reference papers.

Ventilation model

The ventilation model developed by Swan et al. (2012) was used to predict the time-averaged topological distribution of inhaled air in the upright human lung, governed by local tissue deformation, elastic recoil pressure, airway resistance and acinar compliance. Each of the acini in the tree model subtending each terminal bronchiole, and worked as an individual compliant compartment. The acinar volume and compliance were initialised at FRC using a distribution of tissue strain along the gravitational direction that was consistent with strain computed by a tissue mechanics model (Tawhai et al., 2009). A coefficient of variation of 0.1 was added to the acinus volume. Compliance of each acinus was calculated using a relationship between volume and compliance for isotropically expanding units of tissue in the Tawhai et al. (2009) tissue mechanics model:

$$C = \left[\frac{\xi e^\gamma}{6V_0} \left(\frac{3(3a+b)^2(\lambda^2 - 1)^2}{\lambda^2} + \frac{(3a+b)(\lambda^2 + 1)}{\lambda^4} \right) \right]^{-1}, \quad (1.12)$$

where λ is the (isotropic) stretch, V_0 is the undeformed volume, and $\gamma = \frac{3}{4}(3a+b)(\lambda^2 - 1)^2$. The movement of air into each acinar unit was determined by expansion of the alveolar tissue and airway resistance.

In this model, the flow through the conducting airways was assumed to be Poiseuille with a "correction factor" to account for additional energy losses that occur in branching

airways (Pedley et al., 1970). Additional energy losses caused by flow disturbances are created at the airway bifurcations and contribute to the calculation of pressure drop across the junction. A correction term, Z_{Pe} , was used to define the ratio of actual energy dissipation to Poiseuille flow dissipation, then the ratio of actual airway resistance (R_{aw}) to its Poiseuille flow equivalent (R_P) can be calculated by (ignoring kinetic energy changes):

$$Z_{Pe} = \frac{R_{aw}}{R_P} = \frac{K_{Pe}}{4\sqrt{2}} \left(R_e \times \frac{2r}{l} \right)^{0.5}, \quad (1.13)$$

where R_e is the Reynolds number, r and l are the radius and length of the airway, respectively. $R_e = \frac{2Q\rho}{\pi r \mu}$, where ρ and μ are the density ($1.51 \times 10^{-6} g.mm^{-3}$) and viscosity ($1.92 \times 10^{-5} P_a.s$) of air, respectively. K_{Pe} is a constant, set to 1.85. Then, the resistance of each airway branch was calculated as the Poiseuille resistance (R_{aw}) multiplied by the term Z_{Pe} , and the Poiseuille flow through each conducting airway was acquired by the following equation:

$$P_{aw_2} - P_{aw_1} = R_{aw}Q = Z_{Pe}R_PQ = Z_{Pe} \frac{8l\mu}{\pi r^4} Q, \quad (1.14)$$

where P_{aw_1} , P_{aw_2} are the air pressures at the start and end of a branch, and Q is the air flow through the airway. The air flow into the acinus (modelled as a compliant unit subtending the terminal bronchiole) was determined by an equation of motion that relates airway resistance, air flow, tissue compliance and the rate of change of internal and external pressures:

$$P_{aw} = \frac{V_A}{C_A} + R_{aw}Q + I \frac{dQ}{dt} - P_l, \quad (1.15)$$

where P_{aw} , R_{aw} and Q are the pressure, Poiseuille resistance and flow in the terminal bronchiole, V_A and C_A are the volume and compliance of the acinar unit, I is inertance of the unit, and P_l is an external driving pressure (varied sinusoidally) working to expand the unit and drive air flow through the conducting airways to the terminal units.

Here, we assumed that the rate of change of airflow Q is small enough, that the term $I \frac{dQ}{dt}$ in Equation 1.15 can be neglected. A suitable small time interval, $\Delta t = t_n - t_{n-1}$, was defined, and the flow at the end of the time period $Q_n = Q(t_n)$ (Q with respect to t) can be calculated as:

$$Q_n = C_A(\nu - \beta) + Q_{n-1} - C_A(\nu - \beta) \exp\left(\frac{-\Delta t}{R_{aw}C_A}\right), \quad (1.16)$$

where $Q_{n-1} = Q(t_{n-1})$ is the flow at the end of the previous time period. $\nu = dP_{aw}/dt$, and $\beta = dP_l/dt$ are the change of bronchiole pressure and driving pressure with respect to t , respectively. This equation is derived from Equation 1.15. The detailed description can be found in Swan et al. (2012).

Perfusion model

The multi-scale pulmonary perfusion model developed by Clark et al. (2011) was used to simulate a time-averaged distribution of blood flow, capillary blood volume and average red blood cell (RBC) transit time for each acinus unit. The full vascular structure (including arteries, veins, intra-acinar arterioles and venules, and capillaries) generated in Section 1.2.3 was the geometric domain for this model. Distension of blood vessels and hydrostatic effects were also included in the model, with arterial and venous diameter and the thickness of the capillary sheet assumed proportional to the transmural pressure (P_{tm}). The intra-acinar (extra-capillary) blood flow was modeled in the sym-

metric ladder structure introduced previously. The microcirculatory model relates the vessel diameter, length and the thickness of capillary sheet.

Similarly to air flow, the flow through pulmonary arteries and veins was predicted using a Poiseuille equation, with an additional term for gravitational effects acting on blood in the vessels. The relationship is given by:

$$\Delta P = P_{b2} - P_{b1} = \frac{128\mu_b L \dot{Q}}{\pi D^4} + \rho_b L g \cos\theta, \quad (1.17)$$

where P_{b1} and P_{b2} are the blood pressures at the beginning and end of the vessel element, μ_b and ρ_b are the viscosity and density of the blood in the vessel, L and D are the vessel length and radius, \dot{Q} is the volumetric flow rate in the vessel, g is the gravitational acceleration ($9.81 m/s^2$), and θ is the angle between the vessel and the direction of gravity.

The term $\rho_b L g \cos\theta$ in Equation 1.17 represents the effect of gravity on blood in the vessels. In the microcirculatory model, an arteriole and venule were joined at each generation by a capillary bed, forming a "ladder-like" structure, to construct the intra-acinar circulation. Therefore, the term $\rho_b L g \cos\theta$ was considered negligible because the length of acinar arterioles and venules was assumed to be small enough:

$$\Delta P = \frac{128\mu_b L \dot{Q}}{\pi D^4}, \quad (1.18)$$

The strained diameter D in Equation 1.18 was assumed to have a linear relationship with the transmural pressure P_{tm} as:

$$\frac{D}{D_0} = \alpha P_{tm} + 1, \quad (1.19)$$

where D_0 is the unstrained vessel diameter, α is the vessel compliance constant. The tethering pressure acting on the blood vessel in the radial direction was assumed to be equal and opposite to the local tissue elastic recoil pressure (P_e), therefore $P_{tm} \approx P_b - P_e$, where P_b is the average blood pressure along the vessel. Then, the blood flow through a capillary sheet (\dot{Q}) was modelled using the classic sheet flow theory developed by Fung and Sobin (1969):

$$\dot{Q} = \frac{SA}{\mu_c f l_C^2} \int H^3 dP_{tm}, \quad (1.20)$$

where A is the alveolar surface area, S is the proportion of alveolar surface area (A) composed of capillaries, μ_c is the apparent viscosity of blood in the capillaries, f is the numerical friction factor, l_C is the average path length through the capillary network between arteriole and venule. H is the thickness of the capillary sheet which was assumed to be approximately linearly dependent on P_{tm} similar to Equation 1.19:

$$\frac{H}{H_0} = \alpha_C P_{tm} + 1, \quad (1.21)$$

where H_0 is the unstrained sheet thickness. In both Equation 1.19 and Equation 1.21, maximum P_{tm} was assumed to be $32\text{cmH}_2\text{O}(3.1\text{KP}_a)$. α_C is the compliance of the capillary sheet, which was assumed to reduce linearly with increase of transpulmonary pressure (P_{tp}):

$$\alpha_C(P_{tp}) = a + bP_{tp}, \quad (1.22)$$

where a and b are constants, P_{tp} is assumed to be equal and opposite to P_e . The values of a and b were firstly measured for dogs by Glazier et al. (1969), then scaled for human

as $a = 0.165 \mu m/cmH_2O$, $b = -2.58 \mu m/(cmH_2O)^2$.

Gas exchange model

The ventilation and perfusion distribution predicted by the ventilation and perfusion models described in the previous section were used as inputs in a whole lung model of gas transport and exchange. The ventilation model provided the volume change in each acinus during inspiration and expiration. The perfusion model determined the acinar capillary blood volume and average RBC transit time. The modelling was based on the assumption that the acinus was well-mixed, and the ventilation and perfusion distributions were time-invariant. Then the rate of O_2 removal from the alveolar air and the rate of CO_2 transferred to the well-mixed alveolar compartment of the acinus were determined. The steady-state gas transfer model developed by Kapitan and Hempleman (1986) and used by Clark et al. (2014) was used to predict the partial pressure of oxygen in alveolar air ($P_{A}O_2$) and in arterial blood (P_aO_2).

In each gas exchange acinar unit, the steady-state blood and gas compositions are related by conservation of mass. the equilibrium oxygen partial pressure was described through the relationship:

$$\dot{V}_I P_{I_{O_2}} - \dot{V}_E P_{A_{O_2}} = k \dot{Q}_C (C_{C_{O_2}} - C_{\bar{V}_{O_2}}), \quad (1.23)$$

where \dot{V}_I is the unit's inspired ventilation (L/min), $P_{I_{O_2}}$ is the oxygen partial pressure (mmHg) of the humidified inspired air, \dot{V}_E is the expired (alveolar) ventilation (L/min), $P_{A_{O_2}}$ is the oxygen partial pressure (mmHg) of the alveolar air, k is a constant that accounts for differences in temperature and pressure between body and the atmosphere as well as allowing consistency between the units of the left and right hand side of Equa-

tion 1.23, \dot{Q}_C is the capillary blood flow, C_{CO_2} is the oxygen content in the end-capillary blood (ml gas/100 ml blood), and $C_{\bar{V}O_2}$ is oxygen content entering the lungs from mixed venous blood (ml gas/100 ml blood). The O_2 and CO_2 contents are associated with the corresponding partial pressure of O_2 and CO_2 by the appropriate dissociation curve. The left-hand side of Equation 1.23 represents the volume rate of gas uptake from the compartment by the air, and the right-hand side represents the volume rate of gas uptake from the compartment by the blood. The rates are equal at steady-state.

The non-linear Monod-Wyman-Changeaux model (Monod et al., 1965) is used to solve the relationship between oxygen content and partial pressure. The oxygen content in the end-capillary blood C_{CO_2} in each acinus unit is related to the oxygen partial pressure (P_aO_2) as:

$$C_{CO_2} = \frac{15 \times 1.34 \times \rho(P_aO_2) + 0.03 \times P_aO_2}{100}, \quad (1.24)$$

where $\rho(P_aO_2)$ is the oxygen saturation, and it is a function of P_aO_2 . The oxygen binding capacity with haemoglobin is 1.34 mL oxygen per gram of hemoglobin, and around 15 g of hemoglobin per 100 mL of blood. Therefore, the term $15 \times 1.34 \times \rho(P_aO_2)$ expresses oxygen bound to haemoglobin. The term $0.03 \times P_aO_2$ expresses the oxygen dissolved in blood plasma, which gives 0.03 mL of oxygen per 100 mL of whole blood for each mmHg of partial pressure.

The oxygen saturation $\rho(P_aO_2)$ was calculated from Monod-Wyman-Changeaux model (Monod et al., 1965) as:

$$\rho(P_aO_2) = \frac{LK_T\sigma P_aO_2(1 + K_T\sigma P_aO_2)^3 + K_R\sigma P_aO_2(1 + K_R\sigma P_aO_2)^3}{L(1 + K_T\sigma P_aO_2)^4 + (1 + K_R\sigma P_aO_2)^4}, \quad (1.25)$$

where K_R (equals to $3.6 \times 10^6 L/mol^{-1}$) and K_T (equals to $10 \times 10^3 L/mol^{-1}$) are the microscopic dissociation constants of a single ligand bound to a stereospecific site, in the two states (R and T), respectively. L (equals to 171.2×10^6) is the equilibrium constant for the state R to T transition, and σ (equals to $1.4 \times 10^{-6} mol \cdot L^{-1} mmHg^{-1}$) is the oxygen solubility.

In this model, it is assumed that the blood stays in the capillaries long enough to achieve equilibrium state of oxygen between the alveolar air and capillary blood, and P_AO_2 can equilibrate with P_aO_2 at the end of each inspiration. Therefore, P_AO_2 and P_aO_2 can be solved from Equation 1.23 using Newton's method. The ventilation-weighted sum of P_AO_2 was calculated as an estimate of expired oxygen partial pressures from the full lung.

The predicted acinus ventilation and perfusion were used as input into the gas exchange model, and carbon dioxide transport was also simulated using the same assumption of equilibration between air and blood similar to the oxygen transfer model (Kapitan and Happleman, 1986). In each acinus unit, equilibration of carbon dioxide between air side and blood side was represented through a mass balance equation:

$$\dot{V}_A P_A CO_2 = k\dot{Q}_C (C_{CO_2} - C_{\bar{V}CO_2}), \quad (1.26)$$

where \dot{V}_A is the expired or alveolar ventilation, C_{CO_2} is the carbon oxygen content in the end-capillary blood, and $C_{\bar{V}CO_2}$ is carbon oxygen content entering the lungs from mixed venous blood. As the calculation for oxygen exchange, the assumption that time is sufficient to equilibrate between blood and air for carbon oxygen exchange was used, so that P_ACO_2 can be predicted by solving Equation 1.26. P_aCO_2 in each acinus unit was calculated from C_{CO_2} using Henry's law:

$$C_{CO_2} = \frac{M \cdot P_a CO_2}{1 + M \cdot P_a CO_2} (P_a CO_2 - P_v CO_2), \quad (1.27)$$

where M (equals to $23.86 ml \cdot mmHg^{-1}$) is the transfer factor for carbon oxygen across the capillary-alveolar membrane (Chakraborty et al., 2004), and $P_v CO_2$ is the partial pressure of oxygen in mixed venous blood.

Some parameter values used in the ventilation, perfusion and gas exchange models are listed in Table 1.2. More details of the models are introduced in Swan and Tawhai (2010); Swan (2010); Clark et al. (2011); Swan et al. (2012).

1.2.5 Modelling lung function

Ventilation, perfusion and gas exchange models were solved under normal conditions (using lung and airway geometry for older normal people) and diseased conditions (using lung and airway geometry of IPF patients). Individual subject tissue classification from CALIPER was projected to the IPF airway/vessel trees as labelled disease regions to drive the patient-specific functional modelling of IPF, with fibrosis reducing tissue compliance and narrowing vessel radius. The subject-specific tidal volume, cardiac output, oxygen consumption (VO_2) and carbon dioxide consumption (VCO_2) were estimated based on the patient's individual information. Data from PFTs were used as boundary conditions to control the simulations.

Disease region labelling

The different tissue patterns classified by CALIPER were mapped to the individual airway/vessel trees of each subject. For each airway/vessel terminal node, the corresponding tissue pattern it belonged to (surrounded by) was extracted (through finding the tis-

Table 1.2: Parameter values and their source used in computational models

Parameter	Description	Value	Source
K_{Pe}	Pedley correction factor	1.85	Pedley et al. (1970)
p	Air density	$1.15 \times 10^{-6} g.mm^3$	Ideal gas law (37C)
μ	Air viscosity	1.92×10^{-6}	Sutherland's formula (37C)
α	Vessel compliance	$1.49 \times 10^{-4} Pa^{-1}$	Krenz and Dawson (2003)
μ_b	Blood viscosity	$3.36 \times 10^{-3} Pa/s$	Pries et al. (1996)
p_b	Blood density	$1.05 \times 10^{-6} kg/mm^3$	Pries et al. (1996)
μ_c	Apparent viscosity of blood in capillary bed	$1.92 \times 10^{-3} Pa/s$	Fung (2013)
f	Numerical friction factor	21.6	Fung (2013)
α_c	Compliance of capillary sheet	$1.30 \times 10^{-9} Pa/s$	Fung and Sabin (1969)
l_c	Pathlength from arteriole to venue	$11.86 \times 10^{-6} m$	Clark et al. (2010)
K_R	microscopic dissociation constant	$3.6 \times 10^6 L/mol^{-1}$	Monod et al. (1965)
K_T	microscopic dissociation constant	$10 \times 10^3 L/mol^{-1}$	Monod et al. (1965)
L	equilibrium constant	171.2×10^6	Monod et al. (1965)
σ	oxygen solubility	$1.4 \times 10^{-6} mol \cdot L^{-1} mmHg^{-1}$	Monod et al. (1965)
M	transfer factor for carbon oxygen across the capillary-alveolar membrane	$23.86 ml \cdot mmHg^{-1}$	Chakraborty et al. (2004)

sue pattern of the closest voxel to the node), so that each terminal node can be labelled by tissue pattern using an index number. The percentage distribution of each tissue pattern against gravitational height (cranio-caudal axis) quantified in Chapter 4 was also used in the labelling. If the initial labelled amount of disease nodes was less than the cranio-caudal percentage, additional disease regions were added until the cranio-caudal distribution of disease matched the CALIPER classified data. Figure 1.3 shows the disease labelled airway nodes of one patient diagnosed with IPF. Table 1.3 lists the volume percentage of fibrosis (honeycomb + reticular + ground-glass) and emphysema classified by CALIPER software for each time point of these two patients.

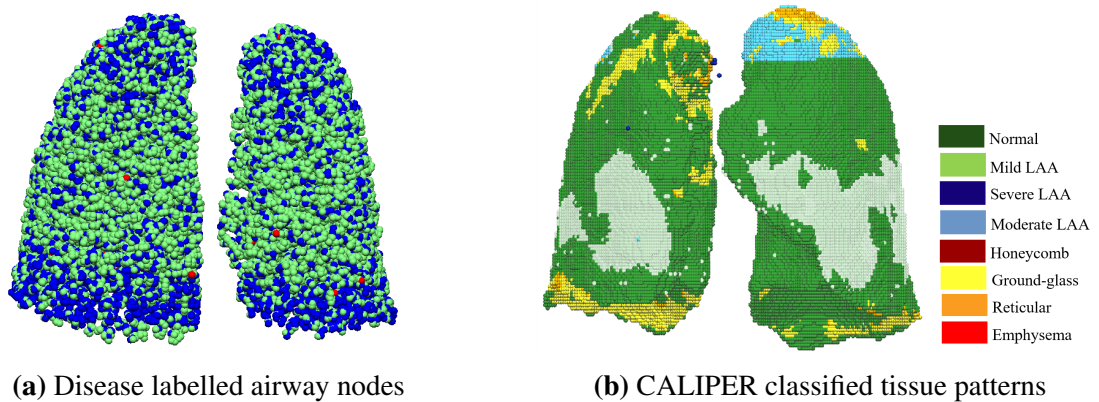


Figure 1.3: Disease labeled airway nodes. Green is classified as normal tissue, blue is fibrosis, and red is emphysema.

Table 1.3: The volume percentage of CALIPER classified disease tissues for each time point of these two patients (%).

Patient No.	Time point	Honeycomb	Reticular	Ground-glass	Total fibrosis	Emphysema
Patient 1	Time point 1	0	6.78	8.84	15.62	0.51
	Time point 2	0.02	4.13	13.62	17.77	0.48
	Time point 3	0.03	3.53	13.05	16.60	0.63
Patient 2	Time point 1	0	1.96	2.42	4.38	0.12
	Time point 2	0.02	4.12	8.58	12.72	0.07

Deep inspiration model

A deep inspiration model was constructed based on the ventilation model (introduced in Section 1.2.4) to simulate a deep inspiration from FRC to TLC. For simulation in the control models, the reference FRC volume (that is the patient-specific predicted normal volume as reference) from PFTs was used as an initial volume to start inspiration, and a subject-specific muscle pressure was solved to drive the lung expansion to the target reference TLC volume (the predicted TLC for the patient). Under the assumption that inspiratory muscle strength does not change with IPF disease (De Troyer and Yernault, 1980), the same driving pressure was used to simulate a deep inspiration in the corresponding IPF model. The IPF models started from their measured FRC. The modelling for IPF patients was divided into two separate stages:

1. The compliance of acini in labelled fibrosis regions (sum of honeycomb, reticular and ground-glass) was reduced to a very low value (less than $0.001 \text{ L/cmH}_2\text{O}$) to represent stiffness due to fibrosis. Then, inspiration was modelled under this initial fibrosis condition.
2. The deep inspiration volume for IPF models acquired in Step 1 was used as the target volume, and the tissue compliance of every acinar unit was scaled down together until the simulated inspiration volume can hit the target, then the corresponding scale factor of total tissue compliance was acquired.

Passive ventilation model

Time-averaged passive ventilation to each acinus over four breathing cycles was predicted using the previously described ventilation model. Acinar volumes in the control and IPF models were initialized to FRC, using the reference normal value and measured

disease value, respectively. The scale factor for acinar tissue compliance identified in Step 2 (above) was applied in the simulation for the IPF patient. Patient-specific tidal volume was estimated based on the patient's weight, gender and height (Gilbert et al., 1972; Pelosi et al., 1998).

Perfusion model

The perfusion model introduced in Section 1.2.4 was used to estimate the distribution of blood. The individual age, weight, height and gender were used to predict the cardiac output for each patient (Brandfonbrener et al., 1955; Miyamura and HONDA, 1973; Stelfox et al., 2006), and the inlet and outlet pressure were adjusted in order to match the estimated cardiac output. Based on previous observations of reduced perfusion in regions of fibrosis (Crystal et al., 1976; Strickland et al., 1993; Plantier et al., 2018), the blood vessel radius in the fibrosis labelled regions were narrowed for IPF models, so that the blood flow would be reduced to the abnormal tissue.

Gas exchange model

The gas transport and exchange were simulated using the gas exchange model introduced in Section 1.2.4. The ventilation and perfusion distribution predicted by the ventilation and perfusion model were used as inputs in the normal and disease condition, respectively. Patient-specific oxygen consumption (VO_2) and carbon dioxide consumption (VCO_2) were estimated using the following equations (Kwan et al., 2004; Coelho-Ravagnani et al., 2013):

$$VO_2 = P_{VO_2} \times W, \quad (1.28)$$

$$VCO_2 = VO_2 \times 0.8, \quad (1.29)$$

where P_{VO_2} is the oxygen consumption at rest ($P_{VO_2} = 2.84 \pm 0.34 \text{ml/kg}^{-1}/\text{min}^{-1}$ for male and $P_{VO_2} = 2.82 \pm 0.37 \text{ml/kg}^{-1}/\text{min}^{-1}$ for female), and W is the weight of the patient (kg).

Using the patient-specific (or control-specific) tidal volume and dead space, and patient- (or control-) specific distribution of \dot{V} and \dot{Q} , the partial pressure of oxygen in alveolar (P_{AO_2}) and in arterial blood (P_{aO_2}) can be predicted using the Kapitan & Happleman gas transfer model (Kapitan and Happleman, 1986).

1.3 Results

1.3.1 Construction of lung lobe geometry

Table 1.4 lists the age, BMI and functional measures used for normal control lung shape prediction for one patient with IPF. The values for FVC, TLC, RV/TLC, and DLCO were predicted reference values from the patient's individual information. Figure 1.4 presents the lung mesh of the IPF patient and its corresponding predicted control lung mesh for the matching normal.

Table 1.4: Predicted reference values used as input to predict a shape model for a normal control.

Parameters	Age	BMI	FVC(L)	TLC(L)	RV/TLC	DLCO(mL/mmHg/min)
Values	82	32.77	3.87	7.22	46	25.1

The average lobe volume proportion for all IPF lung meshes and all predicted control meshes are shown in Table 1.5.

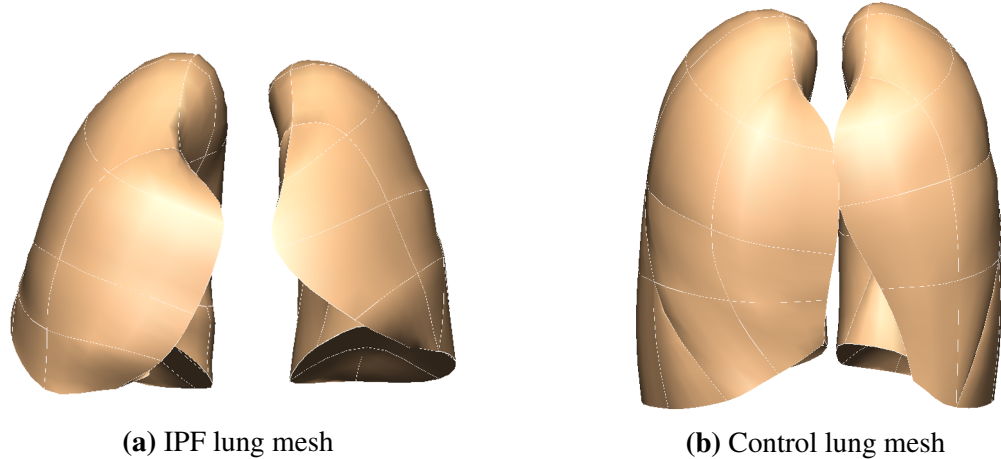


Figure 1.4: Lung mesh for IPF subject and the corresponding predicted lung mesh for a normal control. (a) IPF lung mesh generated from CT imaging of a patient with IPF. (b) Control mesh predicted using the reference values for the same patient.

Table 1.5: Average lobe volume proportion of IPF lung mesh and predicted control lung mesh.

Lobe	IPF	Control
Left lower lobe	0.231	0.242
Left upper lobe	0.290	0.228
Right lower lobe	0.205	0.272
Right middle lobe	0.130	0.078
Right upper lobe	0.144	0.179

As discussed in Chapter 4, Section ??, the shape change in IPF usually relates to a relatively larger anterior-posterior diameter and smaller height of the lung. The IPF lung has a lower average volume proportion for the left lower lobe and right lower lobe compared with normal older subjects. The results illustrated in Figure 1.4 and Table 1.5 are consistent with these previous findings, with the predicted lung mesh for normal controls showing a "thinner" and "elongated" shape and lower average volume of left and right lower lobes compared with the IPF mesh generated from CT imaging.

1.3.2 Construction of airway/vasculature geometry

Airway tree

Figure 1.5 illustrates the generated airway trees of one IPF patient and its corresponding predicted airway tree for the control.

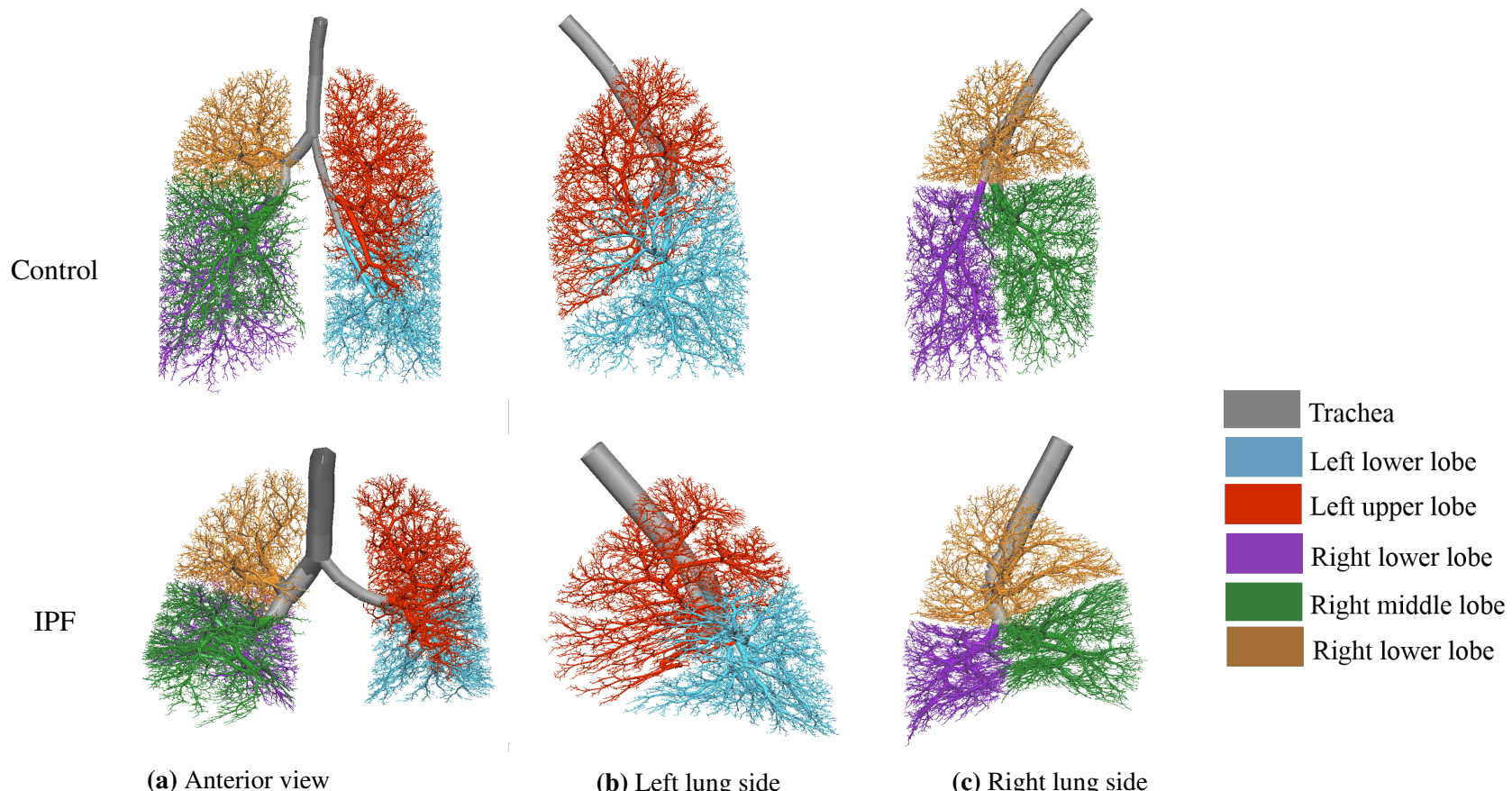


Figure 1.5: Generated normal control airway tree (top row) and IPF airway tree (bottom row) for one patient diagnosed with IPF. (a) Anterior view. (b) Left lung side. (c) Right lung side.

From Figure 1.5, it can be seen that compared with the control airway tree, the IPF airway tree has a larger trachea radius (which is associated with the dilation of the conducting airway in the IPF lung), a relatively smaller lower lobe and a larger anterior-posterior diameter with respect to the cronio-caudal length. These features are consistent with the SSM based analysis result of IPF lung shape in Chapter 4.

Vascular tree

The generated IPF and control artery trees are shown in Figure 1.6. Table 1.6 lists the parameters used for generating the airway tree. Table 1.7 lists the parameters for generating vessel trees.

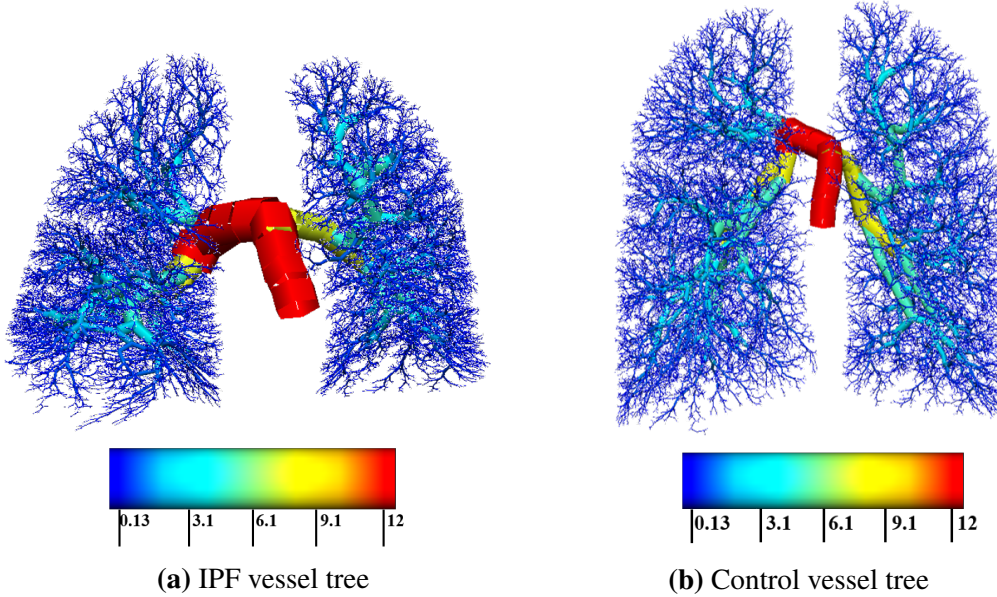


Figure 1.6: Generated geometry of the vessel trees. (a) IPF vessel tree. (b) Control vessel tree. The radius of branches are visualized as shown by the colour bars.

Table 1.6: Parameters of control and IPF airway tree

Patient No.	Time point	Trachea radius (mm)		Horsfield diameter ratio(R_dH)		Terminal radius (mm)		Airway volume (ml)	
		Normal	IPF	Normal	IPF	Normal	IPF	Normal	IPF
Patient 1	Time point 1	6.00	8.81	1.14	1.16	0.20	0.18	76.14	99.80
	Time point 2	6.00	9.82	1.14	1.17	0.20	0.18	75.53	123.87
	Time point 3	6.00	10.03	1.14	1.16	0.20	0.18	74.17	134.84
Patient 2	Time point 1	6.50	9.678	1.14	1.16	0.20	0.18	87.70	110.99
	Time point 2	6.50	8.71	1.14	1.15	0.20	0.18	88.85	111.15

Table 1.7: Parameters of control and IPF vessel tree

Patient No.	Time point	Main artery radius (mm)		Artery R_dS		Main vein radius (mm)		Vein R_dS	
		Normal	IPF	Normal	IPF	Normal	IPF	Normal	IPF
Patient 1	Time point 1	7.69	11.28	1.45	1.51	9.17	14.66	1.48	1.54
	Time point 2	7.69	12.58	1.45	1.52	9.17	16.75	1.48	1.56
	Time point 3	7.69	12.86	1.45	1.52	9.17	17.20	1.48	1.56
Patient 2	Time point 1	8.33	12.40	1.52	1.58	11.18	18.38	1.57	1.65
	Time point 2	8.33	11.16	1.52	1.57	11.18	16.11	1.57	1.63

1.3.3 Deep inspiration modelling

Table 1.8 lists the deep inspiration volumes (from FRC to TLC) for the reference values, simulated, and measured values (from the PFT report). In Table 1.8, the simulated inspiration volume (with CT-based abnormality labelling) at all time points for the two patients are higher than the measured values. That is, loss of compliance in the abnormal (fibrosis) regions on the volumetric CT is not sufficient to explain the reduction in inspiration volume from FRC to TLC in the model, except at time point 3 in patient 1.

Table 1.8: Reference normal, simulated and PFT measured inspiration volume.

Patient No.	Time point	Ref. normal volume	Simulated volume	Measured volume
Patient 1	Time point 1	1.93	1.26	1.16
	Time point 2	1.93	1.27	1.12
	Time point 3	1.84	1.15	1.14
Patient 2	Time point 1	3.4	2.58	2.37
	Time point 2	3.36	2.37	1.93

Additional "fibrosis" was added to the CALIPER classified "normal" tissues until the modelled inspiration volume matched the measured one (as in the last column of Table 1.8). The percentages of CT-based fibrosis (CALIPER classified) and PFT-based fibrosis (CALIPER classified + additional labelled) are listed in Table 1.9.

Table 1.9: Percentage of CT-based fibrosis from CALIPER classification and PFT-based fibrosis (CT-based plus additional fibrosis required to limit inspiration from FRC to TLC).

Patient No.	Time point	CT-based fibrosis (%)	PFT-based fibrosis (%)
Patient 1	Time point 1	17.6	23.7
	Time point 2	18.9	28.9
	Time point 3	22.1	22.9
Patient 2	Time point 1	4.3	11.9
	Time point 2	12.5	29.1

1.3.4 Gas exchange model

Figure 1.7 illustrates the distribution of control, CT-based and PFT-based simulated V/Q ratio and arterial oxygen at one time point for one IPF patient. The figures are shown with V/Q plotted on a logarithmic scale, which is consistent with the presentation of V/Q measurements using the multiple inert gas elimination technique (MIGET). From the results, the simulation for the control model (the first row) predicts a normal V/Q ratio distribution with PaO_2 of 89.33 mmHg; this slightly low PaO_2 is typical for the normal older adult. The model labelled with CT-based fibrosis predicts a characteristic (for IPF) bimodal V/Q distribution (the second row), and PaO_2 considerably decreased (71.63 mmHg) from the control. A slight shift to the left hand side is observed for the highest peak of the V/Q ratio curve compared with the control model. The smaller peak of the V/Q ratio appears around $\text{V}/\text{Q} = 5$ (larger than 1), as there is a decrease in perfusion in fibrotic regions due to the narrowed vessel radius. The model with additional fibrosis (with appropriate patient-specific inspiration from FRC to TLC) predicts further decrease in PaO_2 to 67.85 mmHg.

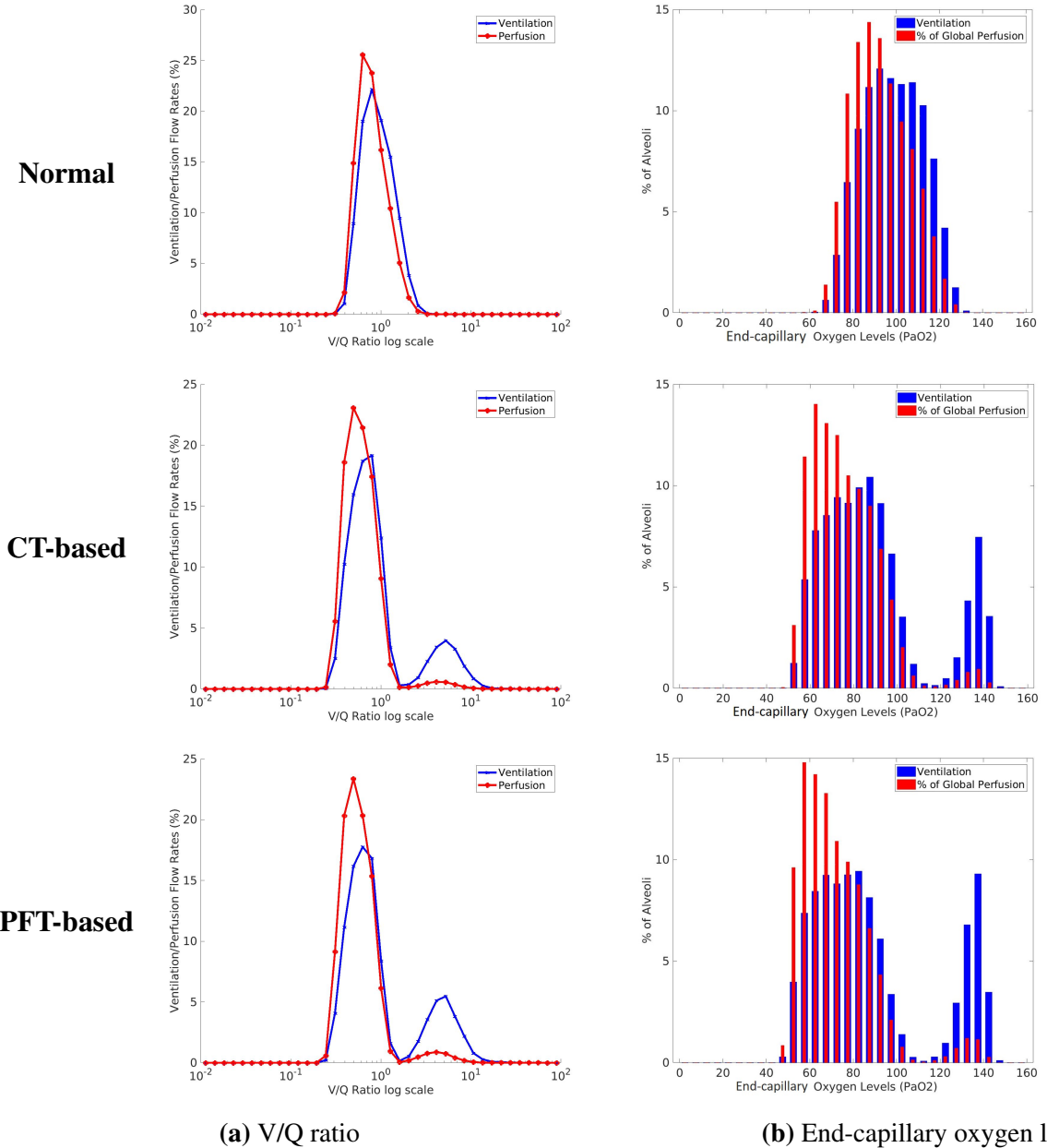


Figure 1.7: V/Q ratio distribution and end-capillary oxygen distribution of control, CT-based and PFT-based simulation result at one time point for one patient diagnosed with IPF). (a) V and Q with respect to V/Q ratio. (b) Distribution of end-capillary oxygen levels amongst alveoli.

Figure 1.8 shows the \dot{V} , \dot{Q} and V/Q ratio distributions against lung height (crano-caudal axis) simulated in the control, CT-based and PFT-based models. For the upright models, \dot{V} is higher in the lung base than apex (Figure 1.8a). The main difference between the control and fibrosis models is a left-wards shift of the \dot{V} curves because of lower total ventilation. The CT- and PFT-based models have very similar \dot{V} . Differences in \dot{Q} are mainly in the basal part of the lung, where more fibrosis appears in the fibrosis models. The two fibrosis models have much higher variability of \dot{Q} within iso-gravitational slices (the error bars in Figure 1.8a and 1.8b) than the control model, particularly in the basal region. For the control model simulation, V/Q ratio is ~ 1 , with a slight increase moving apically.

The values of PaO_2 and PaCO_2 for control, CT-based and PFT-based models for each time point for these two patients are listed in Table 1.10. For CT-based and PFT-based simulation, PaO_2 experiences a decrease over time for both of these two patients, corresponding to the gradual increase of fibrosis. MIGET plots of V/Q ratio and arterial oxygen distribution, plots of crano-caudal distribution of V, Q and V/Q ratio of other subjects and time points can be found in Appendix ??.

Table 1.10: Values of PaO_2 and PaCO_2 of older normal, CT-based and PFT-based modeling results.

Patient No.	Time point	PaO_2 (mmHg)			PaCO_2 (mmHg)		
		Normal	CT-based	PFT-based	Normal	CT-based	PFT-based
Patient 1	Time point 1	89.33	71.63	67.85	41.87	52.73	53.97
	Time point 2	95.37	64.56	58.72	37.81	57.48	59.58
	Time point 3	87.92	60.43	60.00	42.76	59.83	59.97
Patient 2	Time point 1	92.31	88.52	85.13	39.80	41.74	42.86
	Time point 2	91.72	83.70	75.35	39.09	43.77	46.76

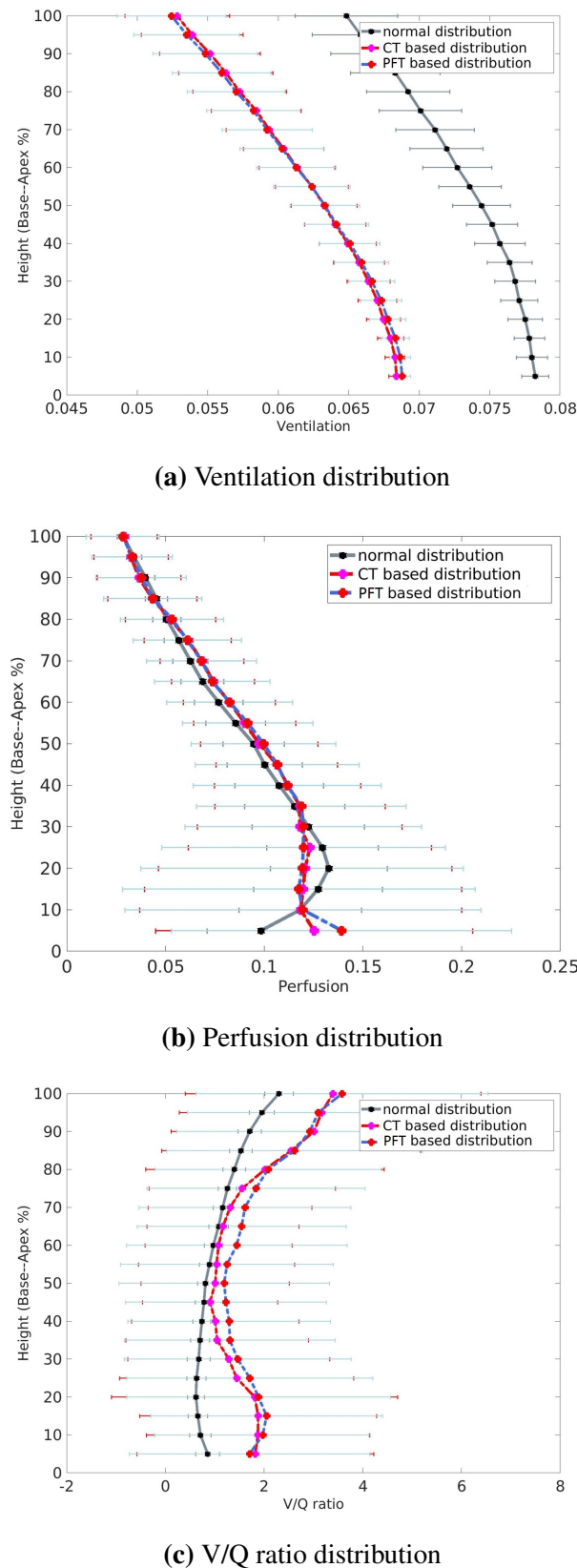


Figure 1.8: Ventilation, perfusion and V/Q ratio distribution against lung height (cranio-caudal axis). (a) Ventilation distribution against lung height. (b) Perfusion distribution against lung height. (c) V/Q ratio distribution against lung height.

1.4 Discussion

In this chapter, a SSM was used to make a prediction of older normal lung shape for each patient. The SSM based lung shape prediction provides a reliable way to make a comparison of the lung function between a patient-specific lung and its corresponding lung of older normal people. The patient-specific shape prediction was achieved based on the patient's individual information which shows significant correlations with older normal lung shape, therefore the estimated lung shape is able to represent the statistical lung shape of older normal people as a control group. Through modelling the airway/vessel tree and lung function with predicted normal lung mesh, it is possible for us to quantitatively describe the change of respiratory geometry in IPF lung, the decline of lung function, the severity of disease and the prognosis of development. That could be a promising direction for clinical applications in the future.

The computational modelling in this chapter shows that the abnormalities classified by CALIPER from volumetric CT imaging may be not sufficient enough to explain the increase in lung stiffness and the decline of lung function in IPF patient. V/Q mismatch (impaired gas exchange) present in CT-based abnormal tissue as well as regions that are classified as 'normal'. This will truly happen in some patients, due to the low quality of CT scan and the errors caused by mis-classification of tissue patterns. Moreover, for the patients diagnosed at the early of the disease, some 'sub-clinical' symptoms that can not be visualized on radiological imaging can definitely damage to the lung function. So, in a sense, our computational modelling method provides a potential way to work as supplement for the radiological and biopsy diagnosis of IPF, and help the clinicians to make a better decision of treatment planning at a earlier stage.

However, there are some limitations of the modelling procedure. First, in IPF lung,

there is a dilation in trachea, but a constriction in small airway. In this chapter, the trachea radius of normal lung was scaled from the trachea radius of IPF lung using a statistically measured ratio which represents the trachea difference between normal and IPF. The main limitation of this method is the measured ratio may be not accurate enough for all the subjects even though the standard deviation has been taken into consideration in our research. A potential direction in the future work could be to use the change of dead space in IPF lung in the construction of airway geometry.

Second, the emphysema and the low attenuation area (LAA) are not taken into consideration in this model. Although emphysema classified by CAPLIPER only covers a small proportion of the lung (usually less than 1%), it is believed to have an impact on the deterioration of lung function together with fibrosis in IPF (Cottin et al., 2005; King Jr et al., 2011; Lin and Jiang, 2015). On the other hand, the LAA (mild, moderate and severe) which accounts for a sizable part of the lung may have some correlation with the appearance of emphysema, and both emphysema and LAA are associated with air trapping at the end of inspiration Slebos et al. (2015); Hoesein and De Jong (2017), which will influence the lung volume at FRC and the change of tissue compliance during breathing. Therefore the emphysema and LAA can to be involved in the future work for setting the initial acinar unit volume at FRC.

Third, for some end-stage subject with a large proportion fibrotic lesion and a small constricted FRC volume, a larger muscle pressure may be needed to drive the expansion of the stiffer lung, thus the deep inspiration volume probably won't be estimated accurately with a normal muscle pressure. In the future study, the chest wall resting volume can be used to help with setting up the tissue compliance in IPF lung, which is calculated by:

$$V_{CWRV} = V_{FRC} + C_{cw} \times (-P_{pl}(FRC)), \quad (1.30)$$

where V_{CWRV} is the chest wall resting volume, V_{FRC} is the FRC volume, C_{cw} is the chest wall compliance (fixed to 0.2 L/cmH₂O) and $P_{pl}(FRC)$ is the pleural pressure at FRC. With a fixed chest wall resting volume for both normal and IPF model, the elastic recoil pressure (P_e) which is determined by pleural pressure will be influenced by the constriction of FRC volume, therefore a correlation can be built between chest wall resting volume and tissue compliance.

1.5 Summary

In this chapter, a patient-specific computational modelling method was developed to investigate the lung geometry and lung function in IPF patient. In order to make a comparison between IPF patient and older normal people, SSM was used to make a prediction of the lung shape of older normal for each patient, and V/Q distribution and gas exchange were then simulated in normal and IPF condition, respectively, with CALIPER tissue classification data and PFT result as input. The result shows that our computational model can reasonably predict the patient-specific ventilation, perfusion and gas exchange in IPF lung, and quantify the difference of lung function between IPF patient and older normal people. Moreover, it is suggested from the result that the CT imaging may be not able to provide enough information to explain the decline of lung function in IPF patient, and the impaired gas exchange will happen in not only abnormal region but also in CT-visualized 'normal' tissues.

List of References

- Arora, N. S. and Rochester, D. F. (1982). Respiratory muscle strength and maximal voluntary ventilation in undernourished patients. *American Review of Respiratory Disease*, 126(1):5–8. [Not cited.]
- Brandfonbrener, M., Landowne, M., and Shock, N. W. (1955). Changes in cardiac output with age. *Circulation*, 12(4):557–566. [Not cited.]
- Brandstetter, R. D. and Kazemi, H. (1983). Aging and the respiratory system. *Medical Clinics of North America*, 67(2):419–431. [Not cited.]
- Breatnach, E., Abbott, G. C., and Fraser, R. G. (1984). Dimensions of the normal human trachea. *American Journal of Roentgenology*, 142(5):903–906. [Not cited.]
- Butler, C. and Kleinerman, J. (1970). Capillary density: alveolar diameter, a morphometric approach to ventilation and perfusion. *American Review of Respiratory Disease*, 102(6):886–894. [Not cited.]
- Chakraborty, S., Balakotaiah, V., and Bidani, A. (2004). Diffusing capacity reexamined: relative roles of diffusion and chemical reaction in red cell uptake of O₂, CO, CO₂, and NO. *Journal of Applied Physiology*, 97(6):2284–2302. [Not cited.]
- Clark, A., Milne, D., Wilsher, M., Burrowes, K., Bajaj, M., and Tawhai, M. (2014). Lack of functional information explains the poor performance of ‘clot load scores’ at

- predicting outcome in acute pulmonary embolism. *Respiratory physiology & neurobiology*, 190:1–13. [Not cited.]
- Clark, A. R., Burrowes, K. S., and Tawhai, M. H. (2010). Contribution of serial and parallel microperfusion to spatial variability in pulmonary inter-and intra-acinar blood flow. *Journal of applied physiology*, 108(5):1116–1126. [Not cited.]
- Clark, A. R., Tawhai, M. H., Hoffman, E. A., and Burrowes, K. S. (2011). The interdependent contributions of gravitational and structural features to perfusion distribution in a multiscale model of the pulmonary circulation. *Journal of applied physiology*, 110(4):943–955. [Not cited.]
- Coelho-Ravagnani, C. d. F., Melo, F. C. L., Ravagnani, F. C., Burini, F. H. P., and Burini, R. C. (2013). Estimation of metabolic equivalent (met) of an exercise protocol based on indirect calorimetry. *Revista Brasileira de Medicina do Esporte*, 19(2):134–138. [Not cited.]
- Cottin, V., Nunes, H., Brillet, P., Delaval, P., Devouassoux, G., Tillie-Leblond, I., Israel-Biet, D., Valeyre, D., Cordier, J., et al. (2005). Combined pulmonary fibrosis and emphysema: a distinct underrecognised entity. *European Respiratory Journal*, 26(4):586–593. [Not cited.]
- Crapo, R. (1993). The aging lung. *Lung biology in health and disease*, 63:1–25. [Not cited.]
- Crystal, R. G., Fulmer, J. D., Roberts, W. C., Moss, M. L., Line, B. R., and Reynolds, H. Y. (1976). Idiopathic pulmonary fibrosis: clinical, histologic, radiographic, physiologic, scintigraphic, cytologic, and biochemical aspects. *Annals of internal medicine*, 85(6):769–788. [Not cited.]
- De Troyer, A. and Yernault, J.-C. (1980). Inspiratory muscle force in normal subjects and patients with interstitial lung disease. *Thorax*, 35(2):92–100. [Not cited.]

- Fung, Y. and Sabin, S. (1969). Theory of sheet flow in lung alveoli. *Journal of Applied Physiology*, 26(4):472–488. [Not cited.]
- Fung, Y.-c. (2013). Biomechanics: circulation. Springer Science & Business Media. [Not cited.]
- Gilbert, R., Auchincloss Jr, J., Brodsky, J., and Boden, W. a. (1972). Changes in tidal volume, frequency, and ventilation induced by their measurement. *Journal of Applied Physiology*, 33(2):252–254. [Not cited.]
- Glazier, J., Hughes, J., Maloney, J., and West, J. (1969). Measurements of capillary dimensions and blood volume in rapidly frozen lungs. *Journal of Applied Physiology*, 26(1):65–76. [Not cited.]
- Guenard, H. and Marthan, R. (1996). Pulmonary gas exchange in elderly subjects. *European Respiratory Journal*, 9(12):2573–2577. [Not cited.]
- Haefeli-Bleuer, B. and Weibel, E. R. (1988). Morphometry of the human pulmonary acinus. *The Anatomical Record*, 220(4):401–414. [Not cited.]
- Hoesein, F. A. M. and De Jong, P. A. (2017). Air trapping on computed tomography: regional versus diffuse. [Not cited.]
- Holland, J., Milic-Emili, J., Macklem, P., and Bates, D. (1968). Regional distribution of pulmonary ventilation and perfusion in elderly subjects. *The Journal of clinical investigation*, 47(1):81–92. [Not cited.]
- Horsfield, K. (1978). Morphometry of the small pulmonary arteries in man. *Circulation research*, 42(5):593–597. [Not cited.]
- Horsfield, K., Dart, G., Olson, D. E., Filley, G. F., and Cumming, G. (1971). Models of the human bronchial tree. *Journal of applied physiology*, 31(2):207–217. [Not cited.]
- Horsfield, K. and Gordon, W. (1981). Morphometry of pulmonary veins in man. *Lung*, 159(1):211–218. [Not cited.]

- Horsfield, K., Relea, F. G., and Gummeling, G. (1976). Diameter, length and branching ratios in the bronchial tree. *Respiration physiology*, 26(3):351–356. [Not cited.]
- Hsia, C. C., Hyde, D. M., and Weibel, E. R. (2016). Lung structure and the intrinsic challenges of gas exchange. *Comprehensive Physiology*, 6(2):827. [Not cited.]
- Huang, W., Yen, R., McLaurine, M., and Bledsoe, G. (1996). Morphometry of the human pulmonary vasculature. *Journal of applied physiology*, 81(5):2123–2133. [Not cited.]
- Janssens, J.-P., Pache, J.-C., and Nicod, L. (1999). Physiological changes in respiratory function associated with ageing. *European Respiratory Journal*, 13(1):197–205. [Not cited.]
- Kapitan, K. S. and Hempleman, S. C. (1986). Computer simulation of mammalian gas-exchange. *Computers in biology and medicine*, 16(2):91–101. [Not cited.]
- King Jr, T. E., Pardo, A., and Selman, M. (2011). Idiopathic pulmonary fibrosis. *The Lancet*, 378(9807):1949–1961. [Not cited.]
- Knudson, R. J., Slatin, R. C., Lebowitz, M. D., and Burrows, B. (1976). The maximal expiratory flow-volume curve: normal standards, variability, and effects of age. *American Review of Respiratory Disease*, 113(5):587–600. [Not cited.]
- Krenz, G. S. and Dawson, C. A. (2003). Flow and pressure distributions in vascular networks consisting of distensible vessels. *American Journal of Physiology-Heart and Circulatory Physiology*, 284(6):H2192–H2203. [Not cited.]
- Kwan, M., Woo, J., and Kwok, T. (2004). The standard oxygen consumption value equivalent to one metabolic equivalent (3.5 ml/min/kg) is not appropriate for elderly people. *International journal of food sciences and nutrition*, 55(3):179–182. [Not cited.]

- Lalley, P. M. (2013). The aging respiratory system—pulmonary structure, function and neural control. *Respiratory physiology & neurobiology*, 187(3):199–210. [Not cited.]
- Larsson, L. (1983). Histochemical characteristics of human skeletal muscle during aging. *Acta physiologica Scandinavica*, 117(3):469–471. [Not cited.]
- Levitzky, M. G. (1984). Effects of aging on the respiratory system. *Physiologist*, 27(2):102–107. [Not cited.]
- Lin, H. and Jiang, S. (2015). Combined pulmonary fibrosis and emphysema (cpfe): an entity different from emphysema or pulmonary fibrosis alone. *Journal of thoracic disease*, 7(4):767. [Not cited.]
- McClaran, S., Babcock, M., Pegelow, D., Reddan, W., and Dempsey, J. (1995). Longitudinal effects of aging on lung function at rest and exercise in healthy active fit elderly adults. *Journal of Applied Physiology*, 78(5):1957–1968. [Not cited.]
- Mittman, C., Edelman, N. H., Norris, A. H., and Shock, N. W. (1965). Relationship between chest wall and pulmonary compliance and age. *Journal of Applied Physiology*, 20(6):1211–1216. [Not cited.]
- Miyamura, M. and HONDA, Y. (1973). Maximum cardiac output related to sex and age. *The Japanese journal of physiology*, 23(6):645–656. [Not cited.]
- Monod, J., Wyman, J., and Changeux, J.-P. (1965). On the nature of allosteric transitions: a plausible model. *Biol*, 12:228–113. [Not cited.]
- Murray, J. F. (1986). The normal lung: the basis for diagnosis and treatment of pulmonary disease. WB Saunders Company. [Not cited.]
- Osanlouy, M. (2018). Statistical Shape Analysis to Quantify Lung Structure-Function Relationships over the Adult Lifespan. PhD thesis, University of Auckland. [Not cited.]

- Paoletti, P., Viegi, G., Pistelli, G., Di Pede, F., Fazzi, P., Polato, R., Saetta, M., Zambon, R., Carli, G., Giuntini, C., et al. (1985). Reference equations for the single-breath diffusing capacity: a cross-sectional analysis and effect of body size and age. *American Review of Respiratory Disease*, 132(4):806–813. [Not cited.]
- Pedley, T., Schroter, R., and Sudlow, M. (1970). Energy losses and pressure drop in models of human airways. *Respiration physiology*, 9(3):371–386. [Not cited.]
- Pelosi, P., Croci, M., Ravagnan, I., Tredici, S., Pedoto, A., Lissoni, A., and Gattinoni, L. (1998). The effects of body mass on lung volumes, respiratory mechanics, and gas exchange during general anesthesia. *Anesthesia & Analgesia*, 87(3):654–660. [Not cited.]
- Plantier, L., Cazes, A., Dinh-Xuan, A.-T., Bancal, C., Marchand-Adam, S., and Crestani, B. (2018). Physiology of the lung in idiopathic pulmonary fibrosis. *European Respiratory Review*, 27(147):170062. [Not cited.]
- Plantier, L., Debray, M.-P., Estellat, C., Flamant, M., Roy, C., Bancal, C., Borie, R., Israël-Biet, D., Mal, H., Crestani, B., et al. (2016). Increased volume of conducting airways in idiopathic pulmonary fibrosis is independent of disease severity: a volumetric capnography study. *Journal of breath research*, 10(1):016005. [Not cited.]
- Pollock, M. L., Mengelkoch, L. J., Graves, J. E., Lowenthal, D. T., Limacher, M. C., Foster, C., and Wilmore, J. H. (1997). Twenty-year follow-up of aerobic power and body composition of older track athletes. *Journal of Applied Physiology*, 82(5):1508–1516. [Not cited.]
- Pries, A., Secomb, T., and Gaehtgens, P. (1996). Biophysical aspects of blood flow in the microvasculature. *Cardiovascular research*, 32(4):654–667. [Not cited.]
- Slebos, D.-J., van Rikxoort, E. M., and van der Bij, W. (2015). Air trapping in emphy-

- sema. *American journal of respiratory and critical care medicine*, 192(5):e45–e45. [Not cited.]
- Smith, T. (1986). Respiratory effects of aging. In *Seminars in Anesthesia*, volume 5, pages 14–22. WB SAUNDERS CO INDEPENDENCE SQUARE WEST CURTIS CENTER, STE 300, PHILADELPHIA, PA 19106-3399. [Not cited.]
- Sprung, J., Gajic, O., and Warner, D. O. (2006). age related alterations in respiratory function—anesthetic considerations. *Canadian journal of anesthesia*, 53(12):1244. [Not cited.]
- Stelfox, H. T., Ahmed, S. B., Ribeiro, R. A., Gettings, E. M., Pomerantsev, E., and Schmidt, U. (2006). Hemodynamic monitoring in obese patients: the impact of body mass index on cardiac output and stroke volume. *Critical care medicine*, 34(4):1243–1246. [Not cited.]
- Strickland, N., Hughes, J., Hart, D., Myers, M., and Lavender, J. (1993). Cause of regional ventilation-perfusion mismatching in patients with idiopathic pulmonary fibrosis: a combined ct and scintigraphic study. *AJR. American journal of roentgenology*, 161(4):719–725. [Not cited.]
- Swan, A. (2010). A multi-scale computational model of pulmonary gas exchange. PhD thesis, University of Auckland. [Not cited.]
- Swan, A. J., Clark, A. R., and Tawhai, M. H. (2012). A computational model of the topographic distribution of ventilation in healthy human lungs. *Journal of Theoretical Biology*, 300:222–231. [Not cited.]
- Swan, A. J. and Tawhai, M. H. (2010). Evidence for minimal oxygen heterogeneity in the healthy human pulmonary acinus. *Journal of applied physiology*, 110(2):528–537. [Not cited.]

- Tawhai, M. H., Hunter, P., Ts chirren, J., Reinhardt, J., McLennan, G., and Hoffman, E. A. (2004). Ct-based geometry analysis and finite element models of the human and ovine bronchial tree. *Journal of applied physiology*, 97(6):2310–2321. [Not cited.]
- Tawhai, M. H., Nash, M. P., Lin, C.-L., and Hoffman, E. A. (2009). Supine and prone differences in regional lung density and pleural pressure gradients in the human lung with constant shape. *Journal of Applied Physiology*, 107(3):912–920. [Not cited.]
- Thurlbeck, W. M. and Angus, G. E. (1975). Growth and aging of the normal human lung. *Chest*, 67(2 Suppl):3S–6S. [Not cited.]
- Turner, J. M., Mead, J., and Wohl, M. E. (1968). Elasticity of human lungs in relation to age. *Journal of applied physiology*, 25(6):664–671. [Not cited.]
- Verbeken, E. K., Cauberghs, M., Mertens, I., Clement, J., Lauweryns, J. M., and Van de Woestijne, K. P. (1992). The senile lung: comparison with normal and emphysematous lungs 1. structural aspects. *Chest*, 101(3):793–799. [Not cited.]
- Wahba, W. (1983). Influence of aging on lung function-clinical significance of changes from age twenty. *Anesthesia & Analgesia*, 62(8):764–776. [Not cited.]
- Weibel, E. R. (1984). The pathway for oxygen: structure and function in the mammalian respiratory system. Harvard University Press. [Not cited.]
- Wijesinghe, M. and Dow, L. (2005). The effect of aging on the respiratory skeletal muscles. *Principles and Practice of Geriatric Medicine*, 2:671–683. [Not cited.]
- Zaugg, M. and Lucchinetti, E. (2000). Respiratory function in the elderly. *Anesthesiology Clinics of North America*, 18(1):47–58. [Not cited.]